

Broddingnagian photon bunching in cathodoluminescence of excitons in WS₂ monolayer

Saskia Fiedler,^{1,*} Sergii Morozov,^{1,2,*} Leonid Iliushyn,^{2,3} Sergejs Boroviks,¹ Martin Thomaschewski,¹ Jianfang Wang,⁴ Timothy J. Booth,^{2,3} Nicolas Stenger,^{2,5} Christian Wolff,¹ and N. Asger Mortensen^{1,2,6}

¹*Center for Nano Optics, University of Southern Denmark, Campusvej 55, DK-5230 Odense M, Denmark*

²*Center for Nanostructured Graphene, Technical University of Denmark, DK-2800 Kongens Lyngby, Denmark*

³*Department of Physics, Technical University of Denmark, DK-2800 Kongens Lyngby, Denmark*

⁴*Department of Physics, The Chinese University of Hong Kong, Shatin, Hong Kong SAR, China*

⁵*Department of Photonics Engineering, Technical University of Denmark, DK-2800 Kongens Lyngby, Denmark*

⁶*Danish Institute for Advanced Study, University of Southern Denmark, Campusvej 55, DK-5230 Odense M, Denmark[†]*

Cathodoluminescence spectroscopy in conjunction with second-order auto-correlation measurements of $g_2(\tau)$ allows to extensively study the synchronization of quantum light sources in low-dimensional structures. Co-existing excitons in two-dimensional transition metal dichalcogenide monolayers provide a great source of identical quantum emitters which can be simultaneously excited by an electron. In this article, we demonstrate large photon bunching with $g_2(0)$ up to 156 ± 16 of a tungsten disulfide monolayer, exhibiting a strong dependence on the electron-beam current density. To further improve the excitation synchronization and the electron-emitter interaction, we show exemplarily that the careful selection of a simple and compact geometry – a thin, monocrystalline gold nanodisk – can be used to realize a record-high bunching $g_2(0)$ of up to 2152 ± 236 . This approach to control the electron excitation of excitons in a WS₂ monolayer allows for the synchronization of quantum emitters in an ensemble, which is important to further advance quantum information processing and computing technologies.

INTRODUCTION

The recent development in the synthesis and the fabrication of two-dimensional (2D) transition metal dichalcogenide (TMDC) monolayers has sparked intensive research of their implementation in applications in the emerging field of quantum information and computing technologies [1, 2]. The family of TMDC monolayers with a thickness of a few atoms provides an attractive combination of optoelectronic properties, including a direct bandgap, a strong spin-orbit coupling and splitting, a spin and valley degrees of freedom [3]. A TMDC monolayer is a high-quality, robust material platform for quantum light generation, where the co-existence of multiple excitons is a resource that represents an ensemble of identical quantum light sources.

Photon statistics and the second-order auto-correlation function $g_2(\tau)$ constitute powerful indicators for the identification of single-photon sources in various solid-state platforms, while also giving insight into the quantum-mechanical correlation between emitters within an ensemble. The spontaneous emission of an individual quantum emitter results in a stream of single photons which exhibits the characteristic dip at zero delay time in the photon-correlation histogram (photon anti-bunching). In contrast, photon statistics of an ensemble formed by identical quantum emitters, localized within a sub-wavelength volume, strongly depends on the excitation synchronization and can exhibit cooperative spontaneous emission (photon bunching) [4].

Photoexcitation of quantum ensembles does not provide the required synchronization as the photon arrival statistics is Poissonian in nature. Therefore, a large ensemble typically exhibits a flat second-order auto-correlation function $g_2(\tau) \rightarrow 1$. To break the $g_2(\tau = 0) = 1$ limit, a high synchronization of emitters is required, and such an ensemble exhibits a peak at zero correlation time, that is $g_2(0) > 1$. The width of the bunching

peak provides information about the emission lifetime of the emitters, while its amplitude indicates the probability of the excitation to interact with an emitter [5].

Photon bunching has been observed, using low-current electron-beam excitation, namely cathodoluminescence (CL) [6]. In the limit of high electron-beam current, the electron arrival approach Poissonian statistics, thus resulting in a flat second-order auto-correlation function $g_2(\tau) \rightarrow 1$ as in the case of photoexcitation. However, reducing the electron-beam current to sub-few hundred pA breaks the Poissonian statistics and an arriving electron will potentially generate multiple identical electron-hole pairs capable of cooperative and synchronized excitation of a quantum ensemble. Exploiting the low currents, various quantum ensembles – such as indium gallium nitride (InGaN) quantum wells and color centers in nano-diamonds – have been shown to generate quantum light with $g_2(0)$ up to 50 [7, 8]. A decrease of the electron-beam current to sub-pA is expected to further increase the $g_2(0)$ -values, however such low currents are unattainable by state-of-the-art instrumentation. Therefore, to further boost the photon bunching, two requirements need to be met, (i) high-quality quantum ensembles consisting of identical and densely localized emitters within a sub-wavelength volume, and (ii) a geometry increasing the probability of electron-emitter interaction.

In this article, we study the luminescence properties and photon statistics of a tungsten disulfide (WS₂) monolayer encapsulated in hexagonal boron nitride (hBN) layers. Using electron-beam excitation, we demonstrate a high photon bunching of $g_2(0) = 156 \pm 16$ which is due to the naturally high quality of WS₂. We further explore methods for improving the excitation synchronization and electron-emitter interaction via adding a monocrystalline gold nanodisk. In such a geometry, we achieve record-high photon bunching of $g_2(0) = 2152 \pm 236$, exceeding the previously reported values by two orders of magnitude.

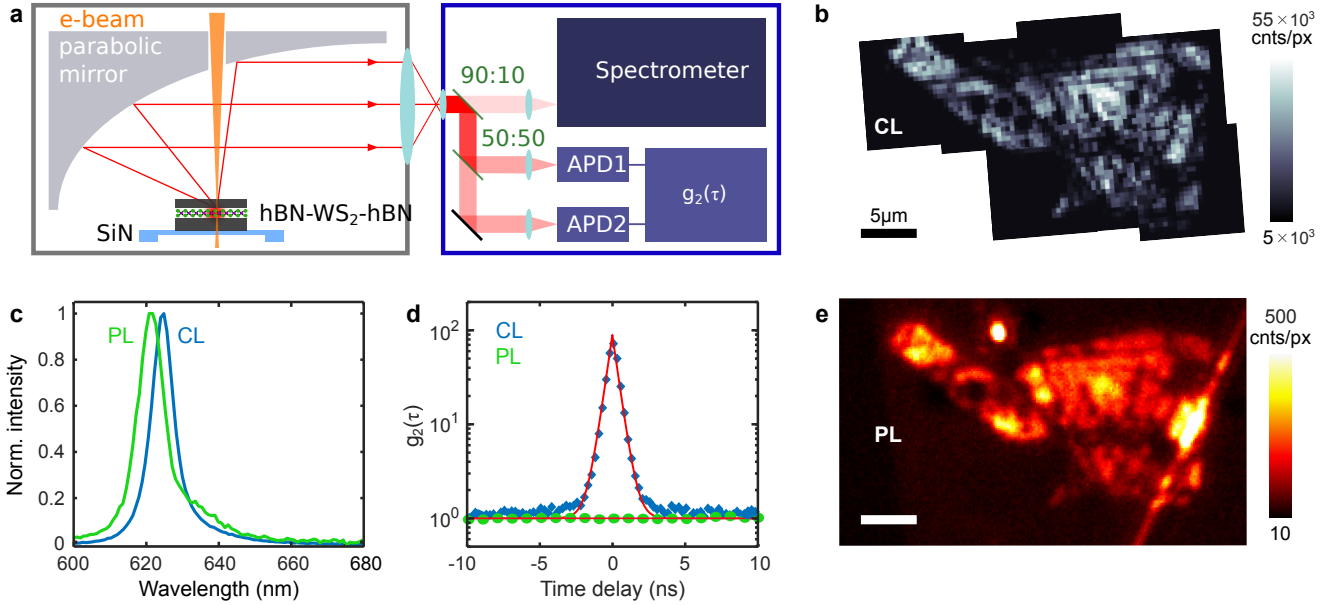


Figure 1. Testing photo- and electron-beam excitation of hBN-encapsulated WS₂ monolayer. **c** Schematics of the experimental setup for detection of electron-beam-induced emission from a WS₂ monolayer. The collected emission is analyzed with a spectrometer and HBT interferometer. **b** CL intensity map obtained by electron-beam scanning of the sample. **c** PL and CL spectra of WS₂-hBN heterostructure. **d** Electron-beam excitation synchronizes emitters and leading to giant photon bunching, while photo excitation is able to generate only a flat $g_2(0) = 1$. **e** PL confocal intensity map of the sample.

Our simple geometry offers a robust and compact platform to generate quantum light with Brodbingnagian [9] photon bunching statistics, which has important applications in quantum information processing and computing technologies.

RESULTS AND DISCUSSION

Sample and experimental setup

We perform photoluminescence (PL) and cathodoluminescence (CL) experiments of a WS₂ monolayer sandwiched between two thin hBN flakes (see details in Methods). The hBN encapsulation on both sides of the WS₂ monolayer serves three purposes: (i) protecting the WS₂ from electron-beam damage and contamination, (ii) increasing the effective interaction volume of incoming electrons with the monolayer, and (iii) providing a layer for the generation of additional charge carriers which can subsequently diffuse into the WS₂ and radiatively recombine, thereby significantly enhancing the CL intensity [10]. Fig. 1a schematically presents the experimental setup for the electron-beam excitation of the hBN-WS₂-hBN sample and the collection of the generated CL. Here, the electron beam is focused onto the hBN-WS₂-hBN stack, and the generated CL is subsequently collimated by a parabolic mirror and focused onto a spectrometer and a Hanbury Brown and Twiss (HBT) interferometer (see Methods).

Photo and electron-beam excitation

Fig. 1b presents a CL intensity map obtained by scanning the electron beam over the hBN-WS₂-hBN sample. The spatial CL distribution reveals areas of lower intensity, most likely cracks in the monolayer as the hBN does not exhibit any luminescence in the visible spectral range (350 nm to 1050 nm). The round dark patches apparent in the CL map can be attributed to bubbles in between the three layers. A lack of adherence of the stacked sample has been shown to result in quenched luminescence [11]. Fig. 1e displays a corresponding PL confocal map obtained with laser excitation at 404 nm. We find a similar intensity distribution as in the CL map in Fig. 1b, although characterized with a lower spatial resolution than with an electron beam.

In Fig. 1c, we compare spectral emission properties of the hBN-WS₂-hBN stack under photo- and electron-beam excitation. The PL spectrum is centered around 621 nm and has a red-shifted satellite peak at 635 nm (green line in Fig. 1c). These emission lines are characteristic for the neutral and red-shifted charged exciton (trion) in WS₂ monolayers at room temperature [12]. In contrast, the CL spectrum in Fig. 1c is dominated by the neutral exciton peak at 626 nm which is red-shifted with respect to the PL spectrum. However, we observe a sub-10 nm spectral wandering of the excitonic peak in both PL and CL measurements which is possibly due to local strain within the WS₂ monolayer [13].

The Photon statistics of the emission generated from the hBN-WS₂-hBN sample drastically depend on the type of excitation. Fig. 1d presents photon correlation histograms obtained

under photo and electron-beam excitation. Electron-beam excitation results in a pronounced photon bunching peak at zero correlation time (blue diamonds in Fig. 1d), while the photon correlation histogram obtained under photo excitation is flat with $g_2(0) = 1$ (green circles in Fig. 1d). Moreover, the bunching amplitude in CL can be tuned by the electron-beam current (which we demonstrate in the next section), unlike the flat photon correlation histogram in PL [6].

The discrepancy between the PL and the CL results can be explained by different excitation mechanisms of the excitons in WS₂. In PL, an incoming photon typically creates one electron-hole pair in the WS₂ monolayer, while an incoming electron can excite many electron-hole pairs in the sample, predominantly in the thicker hBN layers due to a large interaction volume [14]. The latter process can be described by a scattered incoming electron which excites high-energy interband transitions in the sample, also referred to as "bulk plasmons" in electron spectroscopy literature [6, 15, 16]. They subsequently decay into multiple identical electron-hole pairs which, after the typical excitonic lifetime, exhibit synchronized radiative recombination. The photons appear to arrive as a "packet" and can be detected with the HBT interferometer as photon bunching ($g_2(0) > 1$).

CL response to electron-beam current

The CL intensity and the amplitude of photon bunching in CL can be controlled by the electron-beam current I . As the electron-beam current is increased, a higher CL intensity is observed due to the larger amount of incoming electrons, generating more electron-hole pairs in the sample, which can subsequently recombine radiatively in the WS₂ monolayer. The CL spectra collected at varying I , ranging from 3 pA to 211 pA, are shown in Fig. 2a. At higher I (211 pA), the increase of the neutral exciton intensity is accompanied by the appearance of a red-shifted trion peak at 640 nm (violet line in Fig. 2a). In contrast, the photon statistics follow the opposite trend; with increasing I , the synchronization of generated emission is decreased, resulting in a lower photon bunching.

Fig. 2b shows the bunching histograms collected at low and high electron-beam currents, which we fit to extract the values of $g_2(0)$ (see Methods). At the lowest electron-beam current of 3 pA, we achieve a giant bunching factor 156 ± 16 , indicating the high quality of the investigated sample. In contrast, the bunching factor is greatly reduced to approximately 4.7 ± 0.2 for the highest electron-beam current of 211 pA. The I -dependent photon bunching factors are summarized in Fig. 2c. We fit the examined dynamics with $g_2(0, I) = 1 - I_0/I$ as the bunching factor has been observed to be inversely dependent on the applied electron-beam current [6, 16]. Here, I_0 is a free parameter describing the probability of the electron beam interacting with the emitters. The mechanism behind the photon bunching can be attributed to the synchronization of emission from emitters, where each incoming electron creates a photon packet. With increasing electron-beam current, the electrons

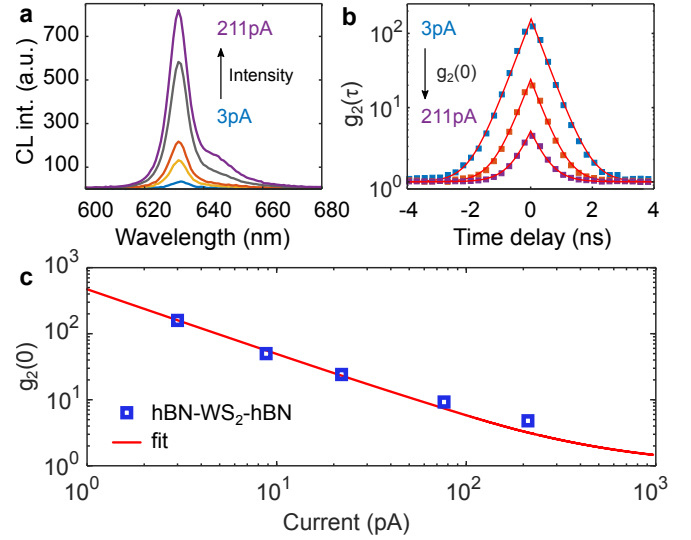


Figure 2. Cathodoluminescence of hBN-encapsulated WS₂ monolayer at low and high electron-beam current. **a** 10 kV-CL spectra demonstrate the growth of CL intensity at increasing electron-beam current. Trion emission accompanies the neutral exciton at the high electron-beam current. **b** Photon correlation histograms show reduction of photon bunching with the increase of electron-beam current. **c** Photon bunching factor $g_2(0)$ is in inverse dependence with the electron-beam current.

arrive closer in time and the photon packets become increasingly indistinguishable, thereby reducing the bunching factor until the Poissonian distribution $g_2(0, \infty) = 1$ is reached. In the hBN-WS₂-hBN-sample, the inverse I -dependence is confirmed in Fig. 2c, although the Poissonian distribution cannot be reached due to sample degradation at high electron-beam currents $I > 250$ pA (see SI).

Boosting bunching through geometry

A further increase of the photon bunching factor by reducing the applied electron-beam current is limited by the instrument. Decreasing the acceleration voltage potentially allows to reduce the current to sub-pA, however in practice, it causes severe sample charging already at 5 kV. To overcome this limit, we suggest to modify the geometry by adding a thin gold nanodisk (ND) to induce a local change of electron beam excitation parameters. We drop-cast monocrystalline gold nanodisks on top of the hBN-WS₂-hBN-stack (see SEM image in SI), whose high quality has been previously confirmed in Ref. [17]. The nanodisks have a diameter ranging from 80 nm to 230 nm. For further CL studies, we chose an Au nanodisk with an approximate diameter of 120 nm, as shown in the inset of Fig. 3a. The reasoning behind this selection is that the (broad) plasmonic dipole mode spectrally overlaps with the WS₂-exciton, in principle, allowing for plasmonic interaction.

Fig. 3a presents the CL spectra of the hBN-WS₂-hBN-stack excited through the 120 nm-Au nanodisk with increasing

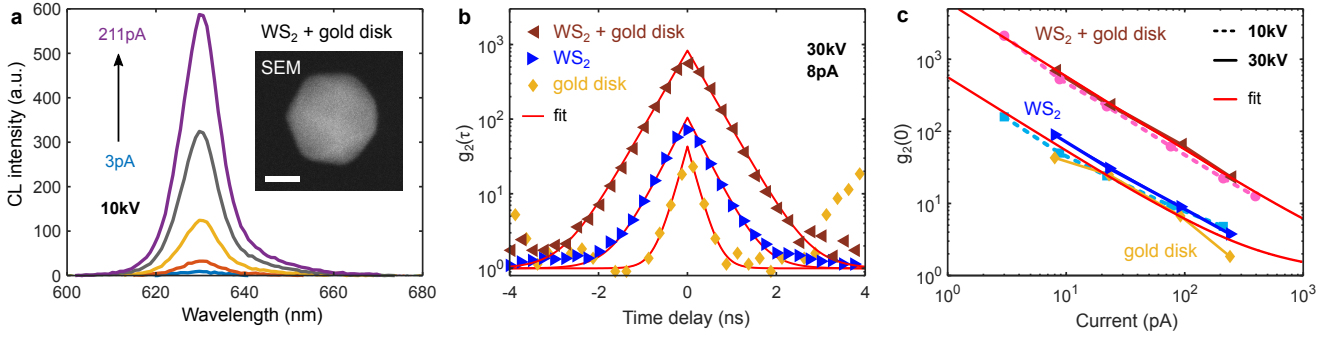


Figure 3. Enhancing electron beam interaction with the sample using a gold nanodisk. **a** 10 kV-CL spectra of hBN-WS₂-hBN excited through a gold nanodisk with 120 nm diameter using electron-beam currents ranging from 3 pA to 211 pA. The inset shows the SEM image of the gold nanodisk. The scale bar is 50 nm. **b** Photon correlation histograms of hBN-encapsulated WS₂ monolayer (blue triangles), hBN-encapsulated WS₂ monolayer with a Au nanodisk on top (dark red triangles), and a similar 120 nm-sized Au nanodisk on hBN (orange diamonds). The electron-beam parameters were held constant at 30 kV and 8 pA. **c** Photon bunching factor ($g_2(0)$) vs. electron-beam current at 10 kV (dashed lines) and 30 kV (solid lines) for the three samples as in **b**.

electron-beam current. We observe an overall CL intensity increase with increasing I , similar to the bare hBN-WS₂-hBN-sample. However, the CL spectra do not reveal any emission enhancement which would indicate a plasmon-assisted Purcell effect, nor any evidence of strong coupling (Fig. 3a). This observation is in agreement with the PL measurements, where the position of the Au nanodisks distributed over the entire hBN-WS₂-hBN-sample cannot be made out. We ascribe this lack of luminescence enhancement to the large separation of 35 nm between the gold nanodisk and the WS₂ monolayer which does not allow for efficient near-field interaction.

Remarkably, the addition of Au nanodisks improves the emission synchronization in the WS₂, and drastically affects the photon bunching factor. The Au nanodisks themselves – on hBN only – exhibit dim CL emission (see spectrum in SI Fig. ??), which allowed us to quantify the bunching factor to $g_2(0) = 50 \pm 0X$ of a similarly sized 120 nm nanodisk (orange in Fig. 3b). Fig. 3b further compares the photon correlation histograms measured at identical excitation parameters (8 pA, 30 kV) from the hBN-WS₂-hBN stack (blue), and a system of a 120 nm-Au nanodisk on hBN-WS₂-hBN-stack (dark red). The fit of the histograms provides information about the lifetime of the generated emission τ_0 and the bunching factor $g_2(0)$. We observe a minor change in emission lifetime of WS₂ after the addition of the Au nanodisk, extracting values of $\tau_{\text{WS}_2} = 365 \pm 18$ ps and $\tau_{\text{WS}_2+\text{Au}} = 416 \pm 10$ ps. Therefore, we conclude that the addition of an Au nanodisk did not facilitate the creation of additional, faster relaxation channels for the WS₂-excitons which is in agreement with the absence of Purcell enhancement. For the bare Au nanodisk, however, we measure a lifetime of $\tau_{\text{Au}} = 196 \pm 34$ ps, which is close to the temporal limit of our setup (180 ps). We also extract a photon bunching factor of 105 ± 11 for the bare hBN-WS₂-hBN-sample, which greatly increases to 829 ± 114 for the system of the 120 nm-Au nanodisk on the hBN-WS₂-hBN-stack at 30 kV. A simple addition of the bare Au nanodisk and the hBN-encapsulated WS₂ bunching factors cannot explain the huge

increase of bunching to 829 ± 114 (which we will focus on in the next section). The highest bunching factor of 2152 ± 236 , we observe at the lowest electron-beam current of 3 pA (at 10 kV) for the Au nanodisk on the hBN-WS₂-hBN-sample (red dashed line in Fig. 3c).

Finally, we confirm the inverse electron-beam current dependence of the photon bunching using a different geometry and a reduced acceleration voltage (from 30 kV to 10 kV) to allow for a further reduction in I . We plot the summary of the results in Fig. 3c, including fits of the $g_2(0, I)$ -data with an inverse current function (red): We extract the following values for $I_0^{\text{WS}_2} = 477 \pm 14$ pA and $I_0^{\text{WS}_2+\text{Au}} = 5257 \pm 154$ pA. The difference in I_0 indicates the change of probability of electrons to interact with the sample due to the presence of an Au nanodisk.

Simulations of electron trajectories

We perform Monte Carlo simulations [18] to shed light on the huge bunching enhancement of the hBN-WS₂-hBN-sample caused by the addition of an Au nanodisk. Fig. 4a,b present the results for electron-beam trajectory simulations of the investigated geometries. In Fig. 4a, similar to the performed experiment, a 10 kV-electron-beam with a spot size of 5 nm penetrates the sample stack (top to bottom): 35 nm hBN, 0.7 nm WS₂, 105 nm hBN, 50 nm SiN. Here, the blue lines represent the primary electrons within the sample stack, while the red ones indicate back-scattered electrons (BSE). At the position of the WS₂ monolayer, marked as a thin green line, the spatial distribution of the primary electrons is almost doubled in size compared to the original 5 nm-electron-beam diameter, which is also illustrated in Fig. 4c, while BSE do not significantly contribute.

In the case of an additional 20 nm-thin gold film on the topmost layer (cf. Fig. 4b), representing the Au nanodisk, the primary electrons are widely scattered within the sample. Consequently, the resulting spread of the electron-beam is

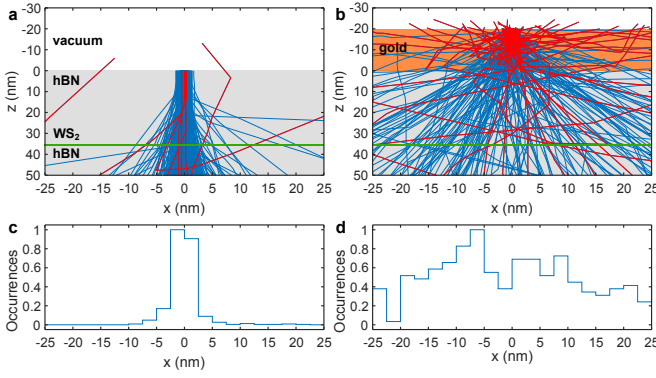


Figure 4. Geometry diverge electron trajectories. **a** Monte Carlo simulation of 10 kV-electron-beam exposure of hBN-WS₂-hBN. Blue and red traces represent primary and back-scattered electrons, respectively. **b** Same simulation as in **a** with a 20 nm Au disk on top of the hBN-WS₂-hBN-stack. **c** Divergence of electron trajectories at the position of WS₂ monolayer (green line in panel **a**). **d** Divergence of electron trajectories at the position of WS₂ monolayer (green line in panel **b**) in presence of a 20 nm-thin Au disk.

enormous. In fact, the divergence is so large that no clear electron-beam diameter can be assigned within the range of 50 nm which is depicted in Fig. 4d. This huge spread of the electron beam reduces the effective electron density at the position of the WS₂ monolayer which is equivalent to a reduced current at a given sample area. As a result, the photon bunching is greatly increased. Ultimately, we conclude that the electron current density determines the photon bunching in CL; not only the temporal distance between incoming electrons plays a crucial role but also the number of electrons within a certain area of the sample. To verify experimentally this important finding, we mimic the spread of the electron beam at the position of the WS₂ monolayer by manually defocusing the electron beam. Here, we increase the working distance which effectively spreads the electron beam to larger spot sizes without changing the initial electron-beam parameters, such as acceleration voltage and current. We observe a similar trend of high photon bunching factors with increasing defocus, while we do not record any substantial change in CL intensity, as shown in Fig. ???. Although this effect of widely spread electrons is by far less pronounced than that of an additional thin Au nanodisk, the trend clearly indicates that the effective electron density at the position of the monolayer governs the resulting photon bunching.

CONCLUSION AND OUTLOOK

In conclusion, we demonstrated the importance of electron-beam excitation for synchronization of large ensembles, and for achieving high photon bunching factors. We reported a high photon bunching ($g_2(0) = 156 \pm 16$) from a WS₂ monolayer encapsulated in hBN in cathodoluminescence. We further suggested that an appropriate geometry can locally

modify the electron-beam interaction with the sample, which allows to boost the photon bunching dynamics far beyond the instrumentation-limited currents. We utilized a system of a 20 nm-thin gold nanodisk on a hBN-WS₂-hBN-stack to demonstrate Brodbingnagian photon bunching of $g_2(0) = 2152 \pm 236$, which is two orders of magnitude larger than previously reported values. Employing Monte Carlo simulations in combination with CL- $g_2(\tau)$ -measurements, we showed that the effective electron current density at the position of the WS₂ monolayer essentially determines the resulting photon bunching factor. We presented a simple way to drive the values of $g_2(0)$ to extremes, which offers a novel quantum source with Brodbingnagian photon bunching for applications in quantum computing information technologies.

METHODS

Sample fabrication. Tungsten disulfide (WS₂) monolayers and hexagonal boron nitride (hBN) flakes with thicknesses from 15 nm to 300 nm were mechanically exfoliated from WS₂ and hBN source crystals (HQ graphene) on oxygen plasma treated silicon (Si) substrates with a 90 nm dry thermal oxide layer (DTU Danchip), using an adhesive tape (Nitto Denko Corp., BT-150E-KL). WS₂ flakes were preselected based on red luminescence under dark-field imaging. hBN-WS₂-hBN heterostructures were assembled using the hot pickup method [19] with incorporated annealing steps to reduce interlayer contamination as follows: prior to the final dropdown of the picked up top-hBN-WS₂, the bottom hBN was annealed in 3% H₂/Ar, 200 sccm for 2 h at 300 °C, 6 mbar. After each stacking step, samples were cleaned on the hBN side in acetone for 1 h, followed by rinsing in distilled water (MilliQ) and isopropyl alcohol (IPA), in order to remove poly(propylene) carbonate (PPC) residue. The assembled heterostructures have finally been annealed in 3% H₂/Ar 200 sccm for 2 h at 600 °C. This step results in the coalescence of any remaining trapped contamination into fewer larger pockets, leaving more contamination free regions for investigation. Completed stacks were then transferred following the methods presented in Ref. 20 onto 50 nm thick silicon nitride (SiN) membrane windows (SIMpore Inc.) for background-free CL investigations.

Cathodoluminescence spectroscopy. Cathodoluminescence (CL) spectroscopy is performed in a Tescan Mira3 scanning-electron microscope (SEM) operated at an acceleration voltage of 10 kV and 30 kV. The electron-beam current is varied from 3 pA to 6.2 nA with an approximate spot size of 5 nm. Light emitted from the sample is collected by a parabolic mirror and analyzed using a Delmic SPARC CL detector equipped with an Andor Newton charge-coupled device (CCD) camera. All CL spectra are corrected for the system response and the background of the thin SiN membrane. CL maps are collected with activated sub-pixel scanning.

CL correlation measurements. For the CL second-order correlation measurements, i.e., the $g_2(\tau)$ correlation function

as a function of the correlation time τ for the temporal CL intensity $I(t)$,

$$g_2(\tau) = \frac{\langle I(t)I(t+\tau) \rangle}{\langle I(t) \rangle \langle I(t+\tau) \rangle} = \frac{\langle I(t)I(t+\tau) \rangle}{\langle I(t) \rangle^2}, \quad (1)$$

a 90:10 beam splitter is inserted before the spectrometer to allow for concurrent spectral and correlation analysis of the sample (see Fig. 1c). 10% of the CL emission is being transmitted onto the spectrometer, while the remaining 90% is being reflected onto a Hanbury Brown and Twiss (HBT) interferometer. Here, the light beam is split by a 50:50 beam splitter, creating a time delay τ between the incoming photons which are detected via two separated avalanche photo diodes (APD, SPCM-AQRH-14-TR, Excelitas Technologies).

We fit experimental time correlation histograms with a current I dependent function: [6]

$$g_2(\tau, I) = 1 - \frac{1}{N} e^{-\tau/\tau_e} + \frac{I_0}{I} \left(1 - \frac{1}{N} \right) e^{-\tau/\tau_e}, \quad (2)$$

where N is an effective number of emitters in the ensemble, τ_e is the emission lifetime, I_0 is a free parameter describing the probability of the electron beam to interact with the emitters in ensemble.

ACKNOWLEDGMENTS

N. A. M. is a VILLUM Investigator supported by VILLUM FONDEN (Grant No. 16498). S. M. acknowledges funding from the Marie Skłodowska-Curie Action (Grant agreement No. 101032967). C. W. acknowledges funding from a MULTIPLY fellowship under the Marie Skłodowska-Curie COFUND Action (Grant agreement No. 713694). The Center for Nanostructured Graphene is sponsored by the Danish National Research Foundation (Project No. DNR103).

* S. F. and S. M. contributed equally to this work.

† asger@mailaps.org

[1] I. Aharonovich, D. Englund, and M. Toth, *Nat. Photon.* **10**, 631 (2016).

- [2] A. Reserbat-Plantey, I. Epstein, I. Torre, A. T. Costa, P. A. D. Gonçalves, N. A. Mortensen, M. Polini, J. C. W. Song, N. M. R. Peres, and F. H. L. Koppens, *ACS Photonics* **8**, 85 (2021).
- [3] S. Manzeli, D. Ovchinnikov, D. Pasquier, O. V. Yazyev, and A. Kis, *Nat. Rev. Mater.* **2**, 17033 (2017).
- [4] V. V. Temnov and U. Woggon, *Opt. Express* **17**, 5774 (2009).
- [5] S. Meuret, *Adv. Imaging Electron Phys.* **215**, 47 (2020).
- [6] S. Meuret, L. H. G. Tizei, T. Cazimajou, R. Bourrellier, H. C. Chang, F. Treussart, and M. Kociak, *Phys. Rev. Lett.* **114**, 197401 (2015).
- [7] M. Solà-Garcia, K. W. Mauser, M. Liebrau, T. Coenen, S. Christiansen, S. Meuret, and A. Polman, *ACS Photonics* **8**, 916 (2021).
- [8] M. A. Feldman, E. F. Dumitrescu, D. Bridges, M. F. Chisholm, R. B. Davidson, P. G. Evans, J. A. Hachtel, A. Hu, R. C. Pooser, R. F. Haglund, and B. J. Lawrie, *Phys. Rev. B* **97**, 081404(R) (2018).
- [9] J. Swift, *Travels into Several Remote Nations of the World. In Four Parts. By Lemuel Gulliver; First a Surgeon, and then a Captain of Several Ships* (1726).
- [10] S. Zheng, J.-K. So, F. Liu, Z. Liu, N. Zheludev, and H. J. Fan, *Nano Lett.* **17**, 6475 (2017).
- [11] G. Nayak, S. Lisi, W. L. Liu, T. Jakubczyk, P. Stepanov, F. Donatini, K. Watanabe, T. Taniguchi, A. Bid, J. Kasprzak, M. Richard, V. Bouchiat, J. Coraux, L. Marty, N. Bendiab, and J. Renard, *Phys. Rev. Materials* **3**, 114001 (2019).
- [12] S. Morozov, C. Wolff, and N. A. Mortensen, *Adv. Opt. Mat.* **9**, 2101305 (2021).
- [13] Z. Li, Y. Lv, L. Ren, J. Li, L. Kong, Y. Zeng, Q. Tao, R. Wu, H. Ma, B. Zhao, D. Wang, W. Dang, K. Chen, L. Liao, X. Duan, X. Duan, and Y. Liu, *Nat. Commun.* **11**, 1151 (2020).
- [14] B. G. Yacobi and D. B. Holt, *Cathodoluminescence microscopy of inorganic solids* (Springer Science+Business Media New York, 1990).
- [15] R. F. Egerton, *Electron energy-loss spectroscopy in the electron microscope* (Springer, New York, 2011).
- [16] S. Meuret, *Intensity interferometry experiment: photon bunching in cathodoluminescence*, edited by M. Hÿtch and P. W. Hawkes, *Advances in Imaging and Electron Physics*, Vol. 215 (Elsevier, 2020) pp. 1–45.
- [17] S. Fiedler, S. Raza, R. Ai, J. Wang, K. Busch, N. Stenger, N. A. Mortensen, and C. Wolff, *Opt. Express* **28**, 13938 (2020).
- [18] D. Drouin, A. R. Couture, D. Joly, X. Tastet, V. Aimez, and R. Gauvin, *Scanning* **29**, 92 (2007).
- [19] F. Pizzocchero, L. Gammelgaard, J. B. S., J. M. Caridad, L. Wang, P. Hone, P. Bøggild, and T. J. Booth, *Nat. Commun.* **7**, 11894 (2016).
- [20] G. F. Schneider, V. E. Calado, H. Zandbergen, L. M. K. Vandersypen, and C. Dekker, *Nano Lett.* **10**, 1912 (2010).